

A strategy for achieving a low-field MRI magnet system with lightweight design and good magnetic field temperature stability

Peng Shen(沈鹏), Jiangqian Guo(郭江黔), Jingzhi Han(韩景智), Ziheng Zhang(张子衡), Xuegang Chen(陈学刚), Wenyun Yang(杨文云), Jie Liu(刘杰), Xianghao Ji(季祥皓), Dong Zhou(周栋), and Jinbo Yang(杨金波)
Citation: Chin. Phys. B, 2026, 35 (**5**): 057503. DOI: 10.1088/1674-1056/ae48bb
http://cpb.iphy.ac.cn; http://iopscience.iop.org/cpb

What follows is a list of articles you may be interested in

Flux trapping behavior in a joint-less closed-loop 2G-HTS coil under multi-pulse magnetic field excitation

Hao Dong(董浩), Daxing Huang(黄大兴), Hao Yu(于昊), Hongwei Gu(古宏伟), and Fazhu Ding(丁发柱)
Chin. Phys. B, 2025, 34 (**7**): 070702. DOI: 10.1088/1674-1056/adcdf0

High-sensitivity spectroscopic measurements under pulsed high magnetic field

Zheng Wang(王政), Yichun Pan(潘议淳), Guangran Yang(杨光冉), Wei Xie(谢微), and Weihang Zhou(周伟航)
Chin. Phys. B, 2025, 34 (**7**): 070701. DOI: 10.1088/1674-1056/adce95

Elastic properties of Cu-6wt% Ag alloy wires for pulsed magnets investigated by ultrasonic techniques

Ziyu Li(李滋雨), Tianyi Gu(顾天逸), Wenqi Wei(魏文琦), Yang Yuan(袁洋), Zhuo Wang(王卓), Kangjian Luo(罗康健), Yupeng Pan(潘宇鹏), Jianfeng Xie(谢剑峰), Shaozhe Zhang(张绍哲), Tao Peng(彭涛), Lin Liu(柳林), Qi Chen(谌祺), Xiaotao Han(韩小涛), Yongkang Luo(罗永康), and Liang Li(李亮)
Chin. Phys. B, 2025, 34 (**2**): 020701. DOI: 10.1088/1674-1056/ada1c8

Process modeling gas atomization of close-coupled ring-hole nozzle for 316L stainless steel powder production

Peng Wang(汪鹏), Jing Li(李静), Hen-San Liu(刘恒三), Xin Wang(王欣), Bo-Rui Du(杜博睿), Ping Gan(甘萍), Shi-Yuan Shen(申世远), Bin Fan(范斌), Xue-Yuan Ge(葛学元), and Miao-Hui Wang(王淼辉)
Chin. Phys. B, 2021, 30 (**5**): 057502. DOI: 10.1088/1674-1056/abd771

Close-coupled nozzle atomization integral simulation and powder preparation using vacuum induction gas atomization technology

Peng Wang(汪鹏), Jing Li(李静), Xin Wang(王欣), Heng-San Liu(刘恒三), Bin Fan(范斌), Ping Gan(甘萍), Rui-Feng Guo(郭瑞峰), Xue-Yuan Ge(葛学元), and Miao-Hui Wang(王淼辉)
Chin. Phys. B, 2021, 30 (**2**): 027502. DOI: 10.1088/1674-1056/abc167

A strategy for achieving a low-field MRI magnet system with lightweight design and good magnetic field temperature stability

Peng Shen(沈鹏)[1,5,6,7], Jiangqian Guo(郭江黔)[2], Jingzhi Han(韩景智)[1,†], Ziheng Zhang(张子衡)[3,8], Xuegang Chen(陈学刚)[4,‡], Wenyun Yang(杨文云)[1], Jie Liu(刘杰)[2], Xianghao Ji(季祥皓)[4], Dong Zhou(周栋)[5,7], and Jinbo Yang(杨金波)[1,§]

[1] *Institute of Condensed Matter and Material Physics, School of Physics, Peking University, Beijing* 100871, *China*
[2] *NingBo ChuanShanjia Electrical and Mechanical Co., Ltd., Yuyao* 315699, *China*
[3] *Beijing Ri-Bei Technology Co., Ltd., Beijing* 102299, *China*
[4] *Center of Free Electron Laser and High Magnetic Field, State Key Laboratory of Opto-Electronic Information Acquisition and Protection Technology, Anhui Provincial Key Laboratory of Magnetic Functional Materials and Devices, Anhui University, Hefei* 230601, *China*
[5] *Central Iron and Steel Research Institute, Beijing* 100083, *China*
[6] *Hefei Gangyan Rare Earth Permanent Magnetic Material Research Institute Co., Ltd., Hefei* 230041, *China*
[7] *State Key Laboratory of Rare Earth Permanent Magnetic Materials, Hefei* 230041, *China*
[8] *Beijing MagnVue Medix Co., Ltd., Beijing* 101111, *China*

(Received 4 December 2025; revised manuscript received 9 February 2026; accepted manuscript online 23 February 2026)

We developed a low field MRI magnet system utilizing a hybrid magnetic circuit composed of sintered neodymium iron boron (Nd–Fe–B) magnet and sintered samarium cobalt (Sm–Co) magnet based on the theoretical simulations. The static magnetic field of the magnet system with a magnetic pole plate diameter of 58 cm and a distance of 32 cm between the upper and lower pole plates reaches 0.07 T and exhibits magnetic field inhomogeneity fluctuations of less than 850 ppm over a temperature variation of ±4 °C around the set point of 24 °C. While it merely weighs 384 kg. Our findings indicate that a hybrid magnetic circuit composed of these two types of magnets contributes to both the lightweight design and temperature stability of the MRI magnet system. Finally, we evaluated the imaging effects of this magnet system.

Keywords: low-field MRI, hybrid magnetic circuit, lightweight, magnetic field temperature stability

PACS: 75.50.Ww, 07.55.Db, 41.20.Gz, 07.55.–w

DOI: 10.1088/1674-1056/ae48bb **CSTR:** 32038.14.CPB.ae48bb

1. Introduction

The greatest advantage of magnetic resonance imaging (MRI) is that it is currently one of the few clinical diagnostic methods that are safe, fast, accurate, and cause no harm to the human body.[1,2] Although high magnetic field MRI can achieve high image resolution, which aids in disease diagnosis, its high production and maintenance costs result in a limited number of such devices, making it difficult to meet the timely diagnosis of disease. Therefore, the research and development of low-cost permanent magnet MRI systems has remained a key focus in the field.[3–12]

Permanent magnet MRI systems offer advantages such as low cost, including reduced maintenance expenses, low failure rates, and minimal energy consumption.[3,4] However, traditional middle-field (greater than 0.3 T) or high-field (greater than 1 T) permanent magnet MRI devices are relatively bulky (weighing over 1 ton) and difficult to move. While low-field (less than 0.3 T) permanent magnet MRI systems can achieve lightweight designs, their limited image resolution has hindered their practical application. In recent years, advancements in artificial intelligence technology have significantly improved the imaging quality of low-field permanent magnet MRI, making it feasible to use low-field MRI for disease diagnosis and treatment.

Currently, the static magnetic field in the low-field permanent magnet MRI systems under research and development is primarily composed of either sintered neodymium iron boron (Nd–Fe–B) magnets or sintered samarium cobalt (Sm–Co) magnets as single materials. Although sintered Nd–Fe–B magnets possess a high remanence (exceeding 1.45 T), which contributes to the lightweight, they suffer from poor temperature stability, such as a relatively low Curie temperature (approximately 312 °C) and an undesirable remanence temperature coefficient (around −0.11%/°C).[13–16] As a result, when used in low-field permanent magnet MRI systems, the impact of temperature variations caused by alternating magnetic fields and environmental conditions on imaging quality must be carefully considered. In contrast, sintered Sm–Co magnets

†Corresponding author. E-mail: hanjingzhi@pku.edu.cn
‡Corresponding author. E-mail: xgchen@ahu.edu.cn
§Corresponding author. E-mail: jbyang@pku.edu.cn

© 2026 Chinese Physical Society and IOP Publishing Ltd. All rights, including for text and data mining, AI training, and similar technologies, are reserved.

exhibit excellent temperature characteristics, including a high Curie temperature (approximately 800 °C) and a favorable remanence temperature coefficient (around −0.03%/°C).[17] Low-field MRI systems constructed with Sm–Co magnets generally do not require concern over the effects of ambient temperature changes on magnetic field stability or imaging quality. However, their remanence is relatively low (approximately 1.1 T), which is only about 60% of that of sintered Nd–Fe–B magnets. Consequently, MRI magnet systems built with sintered Sm–Co magnets remain bulky, with a typical weight of around 700 kg. Therefore, the research and development of lightweight or movable low-field permanent magnet MRI systems with good temperature stability has become a current focal point in the field.[18–22]

This work integrates the respective advantages of sintered Nd–Fe–B magnets and sintered Sm–Co magnets. Based on theoretical simulation and analysis, we have researched and developed a low-field lightweight MRI magnet system composed of both sintered Nd–Fe–B and Sm–Co magnets. This hybrid magnet system combines the benefits of lightweight design and good temperature stability of the magnetic field. Finally, we evaluated its imaging effects.

2. Simulation and experiment

The Nd–Fe–B magnets, Sm–Co magnets and yoke were supplied by Baotou INST Magnetic Material Co., Ltd. (Baotou, China), the Central Iron and Steel Research Institute (CISRI, China) and Ningbo Chuansanja Electromechanical Co., Ltd. (China), respectively. The Nd–Fe–B magnets exhibit a remanence of 1.475 T and a temperature coefficient of −0.11%/°C, while the Sm–Co magnets have a remanence of 1.185 T and a temperature coefficient of −0.03%/°C. The yoke exhibits a saturation magnetic flux density of 2.1 T.

In order to obtain the MRI magnet systems composed of both sintered Nd–Fe–B and Sm–Co magnets, magnetic field simulations of the static magnetic field were performed using COMSOL Multiphysics. Based on the above simulation, the magnetic circuit design scheme corresponding to the size and the magnetic field of the MRI magnet system were obtained, and the specific shapes and sizes of the two magnets and the yoke were also obtained. On this basis, the magnet system was processed and manufactured. The uniformity of its static magnetic field with temperature was investigated using a nuclear magnetic resonance magnetometer. To investigate its imaging effect, the corresponding gradient coils and RF coils were also designed and manufactured, and a spectrometer produced by MR Solution Company was employed.

3. Results and discussion

The research objective of this work is to develop a magnet system with a pole disk diameter of 58 cm and a pole disk spacing of 32 cm. A static field strength of 0.07 T is required, with inhomogeneity maintained below 1000 ppm across a 20-cm diameter spherical volume (DSV) centered on the system. Moreover, the magnet system needs to be as lightweight as possible and possess good temperature stability. In order to obtain the above MRI magnet systems, magnetic field simulations of the static magnetic field were firstly performed using COMSOL Multiphysics. To simplify the calculations, the initial simulations only considered the influence of the magnetic properties of sintered NdFeB magnets and sintered SmCo magnets on the weight and temperature characteristics of the magnetic system. The design schemes for a hybrid magnetic circuit composed of Nd–Fe–B and Sm–Co magnets were mainly discussed, and those for magnetic circuits composed of a single Nd–Fe–B magnet and a single Sm–Co magnet were also discussed for comparisons.

Figure 1 illustrates the magnet layout used in this simulation. Both the upper and lower pole plates, with a diameter of 58 cm and separated by a gap of 32 cm, consist of seven concentric rings. The selection of a seven-ring structure is based on considerations of practical machining difficulty and the achievement of high magnetic field uniformity. In the simulation process, each ring is made of the same material. The ratios of the number of rings made of Sm–Co to those made of Nd–Fe–B are 7:0 (S7N0), 6:1 (S6N1), . . . , 1:6 (S1N6), and 0:7 (S0N7), respectively. Additionally, considering that the target region is primarily located at the center of the MRI magnet system, the rings made of Sm–Co are placed in the central region of the magnet system. This arrangement leverages their excellent temperature stability to mitigate the impact of the detected object's temperature on the magnetic field's strength and uniformity.

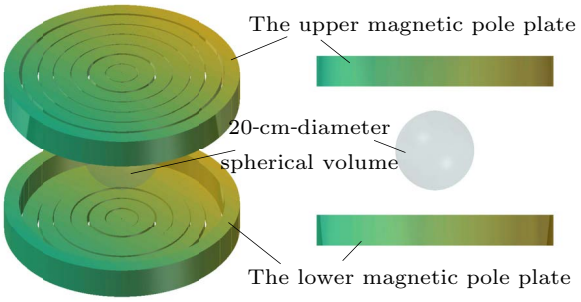


Fig. 1. The structural schematic diagram of the upper and lower magnetic pole plates in the magnet system without the yoke, along with the spherical space with the diameter of 20 cm in the central region between the magnetic pole plates.

We first simulated the total weight of magnets required to generate a static magnetic field of about 0.07 T in the hybrid MRI magnet system with the above spatial constraints.

Figure 2 presents the magnet weight required to generate a magnetic field of approximately 0.07 T using a different magnetic circuit design. It can be seen that the sintered Sm–Co magnet requires more weight due to its lower remanence, whereas the sintered Nd–Fe–B magnet requires less weight

due to its higher remanence. Specifically, for a magnetic circuit composed solely of sintered Sm–Co magnets, 224.3 kg of sintered magnets are required. For hybrid magnetic circuits composed of both sintered Nd–Fe–B and Sm–Co magnets, the total weight of sintered Nd–Fe–B and Sm–Co magnets gradually decreases as the proportion of Nd–Fe–B magnets in the hybrid circuit rises. For a magnetic circuit composed solely of sintered Nd–Fe–B magnets, merely 167.2 kg of sintered Nd–Fe–B magnets are required. These results demonstrate that using hybrid magnetic circuits indeed helps reduce the weight of the upper and lower pole plates and the whole magnet system compared with using single Sm–Co magnetic circuit.

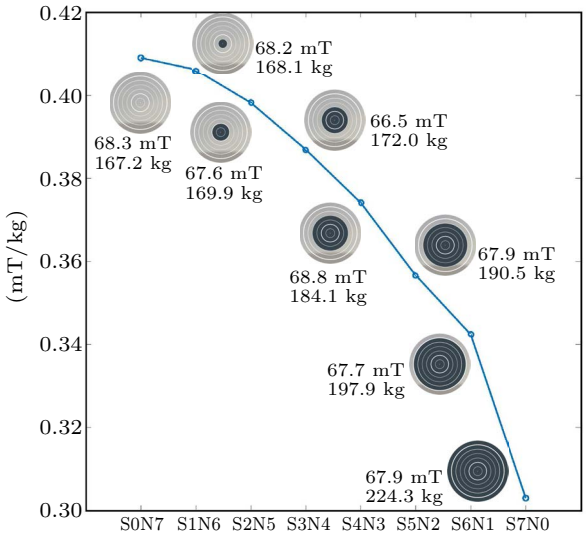


Fig. 2. The magnet weight required to generate a magnetic field of approximately 0.07 T using: a single sintered Nd–Fe–B magnetic circuit, a single sintered Sm–Co magnetic circuit, and hybrid magnetic circuits composed of the two materials in varying proportions.

Since the uniformity of the static magnetic field's response to temperature changes is crucial for subsequent imaging, we investigated how the hybrid magnetic field's uniformity varies with temperature. The specific results are shown in Fig. 3.

The variation of magnetic field inhomogeneity with temperature was shown in Fig. 3. When the upper and lower magnetic pole plates are entirely composed of sintered Nd–Fe–B magnets, the magnetic field exhibits poorer temperature stability due to the material's moderate remanence temperature coefficient of approximately $-0.11\%/^{\circ}\mathrm{C}$. For instance, when a temperature inhomogeneity of 4 °C exists within the magnet system, the magnetic field inhomogeneity at the boundary of the 20-cm diameter spherical space in the central region increases by approximately 1400 ppm. In contrast, when the upper and lower magnetic pole plates are entirely composed of sintered Sm–Co magnets, the magnetic field demonstrates superior temperature stability owing to the material's excellent remanence temperature coefficient of $-0.03\%/^{\circ}\mathrm{C}$. For example, with the same temperature inhomogeneity of 4 °C exists within the magnet system, the variation in boundary magnetic field inhomogeneity is approximately 480 ppm, which is only $\sim 35\%$ of that observed with the sintered Nd–Fe–B magnets. When hybrid magnetic circuits composed of both sintered Nd–Fe–B and Sm–Co magnets are employed for the upper and lower magnetic pole plates, the fluctuation in boundary magnetic field inhomogeneity gradually decreases as the proportion of sintered Sm–Co magnets in the hybrid configuration increases. This demonstrates that the use of hybrid magnetic circuits indeed contributes to improving the temperature stability of the magnetic field compared with single Nd–Fe–B magnetic circuit.

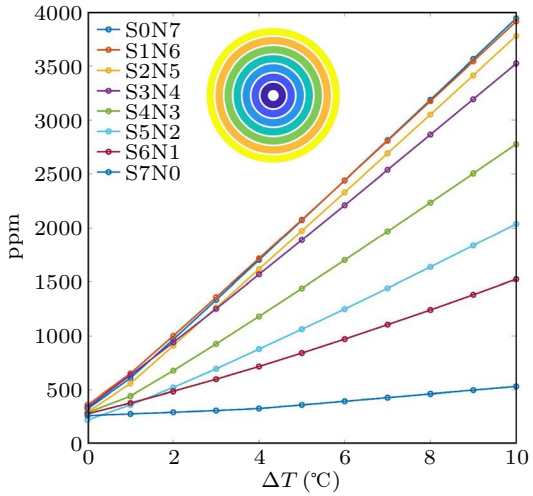


Fig. 3. The variation of magnetic field inhomogeneity at the boundaries of a 20-cm diameter spherical space in the central region of different magnetic circuits with temperatures.

According to the above simulation results, it can be inferred that the hybrid magnetic circuit can integrate the respective advantages of sintered Nd–Fe–B magnets and sintered Sm–Co magnets, enabling the magnet system to achieve relatively balanced performance in terms of both weight and magnetic field temperature stability. For example, with the configuration of the upper and lower magnetic pole plates composed of 5 concentric rings of Sm–Co magnets in the central region and 2 concentric rings of Nd–Fe–B magnets in the peripheral region, only a total of 190.5 kg of Nd–Fe–B and Sm–Co magnets is required to generate a magnetic field of 0.07 T, while maintaining a boundary magnetic field inhomogeneity of 800 ppm with a temperature change of ± 4 °C.

The hybrid magnet system consisting of 5 concentric rings of Sm–Co magnets and 2 concentric rings of Nd–Fe–B magnets would be built up. To enhance its cost-effectiveness and mechanical stability, a rectangular mechanical structure was adopted, and pure iron was utilized as the yoke connecting the upper and lower magnetic pole plates, as seen in Fig. 4. This yoke not only enhances the magnetic field strength and uniformity but also ensures the mechanical stability of the magnet system except for the low price.

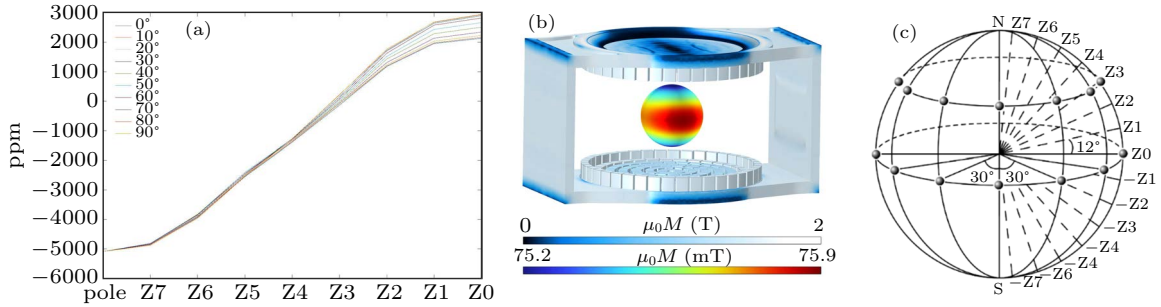


Fig. 4. The magnetic field simulation results obtained using COMSOL software. (a) The magnetic field inhomogeneity across different regions from Z0 to Z7 on the surface of the spherical volume. (b) The magnetic field in various regions of the rectangular-frame magnet system with a hybrid magnetic circuit composed of sintered NdFeB magnets, sintered SmCo magnets and yoke. (c) Diagram of positions Z0, Z1, Z2, ..., Z7, with an angular separation of 12° between adjacent positions.

In order to determine the specific dimensions of the magnets and yoke, the further simulation and modeling of the magnetic field for this rectangular hybrid magnet system using Comsol software was executed. During the simulation process, a 5-mm gap is maintained between magnets of different rings, while a 3-mm gap is kept between magnets within the same ring. This independent or isolated magnet arrangement helps prevent the generation of large eddy currents within the magnets during gradient coil operation, thereby avoiding magnetic field fluctuations caused by temperature rise in the magnets. By continuously optimizing the magnetic field magnitude at the boundary of the 20-cm spherical space between the pole plates, the specifications and dimensions of the sintered Nd–Fe–B and Sm–Co magnets corresponding to a boundary magnetic field inhomogeneity of $\sim$ 8000 ppm were ultimately determined, as shown in Fig. 4. The specifications of the two peripheral rings of sintered Nd–Fe–B magnets in the hybrid magnetic circuit are shown in Fig. S1 of the supplementary materials, while the specifications of the five central rings of sintered Sm–Co magnets are illustrated in Fig. S2 of the supplementary materials. A total of 50 pieces of sintered Nd–Fe–B magnets in specification A1, 34 pieces in A2, and 66 pieces in B, as well as 58 pieces of sintered Sm–Co magnets in specification C, 50 pieces in D, 34 pieces in E, 26 pieces in F, and 10 pieces in G are required.

Figure 5 shows the ultimately constructed low-field MRI magnet system composed of two rings of sintered Nd–Fe–B magnets and five rings of sintered Sm–Co magnets. The system achieves a magnetic field of 0.07 T. At the set operating temperature of 24 °C, the magnetic field inhomogeneity over a 20-cm diameter spherical space is 580 ppm. Regarding temperature performance, when the temperature varies within ±4 °C around 24 °C, the maximum boundary magnetic field inhomogeneity reaches only 1413 ppm, corresponding to an increase of less than 833 ppm. The system utilizes $\sim$ 41 kg of sintered Nd–Fe–B magnets and $\sim$ 33 kg of sintered Sm–Co magnets. The yoke and other auxiliary components weigh 310 kg, resulting in a total system weight of less than 400 kg. This shows that the magnet system achieves relatively balanced performance in terms of both weight and magnetic field temperature stability using hybrid magnetic circuit.

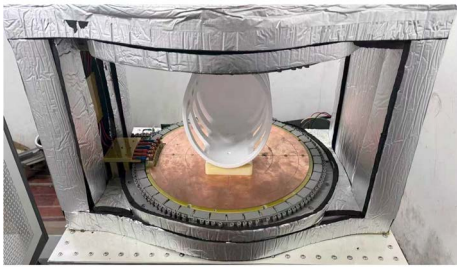


Fig. 5. The assembly structure diagram of a low-field MRI magnet system with a hybrid magnetic circuit composed of sintered Nd–Fe–B and Sm–Co magnets, generating a magnetic field strength of 0.07 T.

Table 1. Variation in magnetic field inhomogeneity with temperature at the 20-cm diameter spherical boundary of the constructed magnet system.

Temperature (°C)	20	22	24	26	28
Inhomogeneity (ppm)	1413	862	580	761	1139

The core mechanism of this hybrid magnetic circuit design of low-field MRI magnet system lies in the coordinated optimization of magnetic material properties and spatial arrangement to achieve a balance between magnetic field strength and temperature stability within the limited space with a pole disk diameter of 58 cm and a pole disk spacing of 32 cm. Specifically, the magnets are configured in concentric rings: the inner five rings consist of Sm–Co magnets, which exhibit excellent temperature stability, owing to their low remanence temperature coefficient, though with relatively lower remanence; the outer two rings are made of Nd–Fe–B magnets, which provide very high remanence but poorer thermal stability. Because the inner-ring magnets are positioned closer to the spherical space, they contribute more significantly to the uniformity and stability of the central magnetic field. Placing the highly thermal-stable Sm–Co magnets in the inner rings therefore allows them to directly dominate the temperature stability of the magnetic field in the target region. Although the outer Nd–Fe–B rings are located farther away and have a lesser influence on the magnetic field in the spherical space, their exceptionally high remanence effectively enhances the mag-

netic field strength at Z0. Through the distance attenuation effect, the relative contribution of the outer Nd–Fe–B magnets to the central magnetic field is reduced, thereby diminishing the impact of their inherent temperature sensitivity on the overall temperature stability of the magnetic field within the spherical space. As a result, a homogeneous low-field magnet system with good temperature stability is achieved without compromising the objectives of light weight and cost control.

Figure 6 demonstrates the imaging effect of an MRI magnet system composed of hybrid magnetic circuits using MRI solution. From the figure, it can be seen that the imaging area of the head has good contrast and resolution. This indicates that the scheme of constructing an MRI magnet system through hybrid magnetic circuits is feasible.

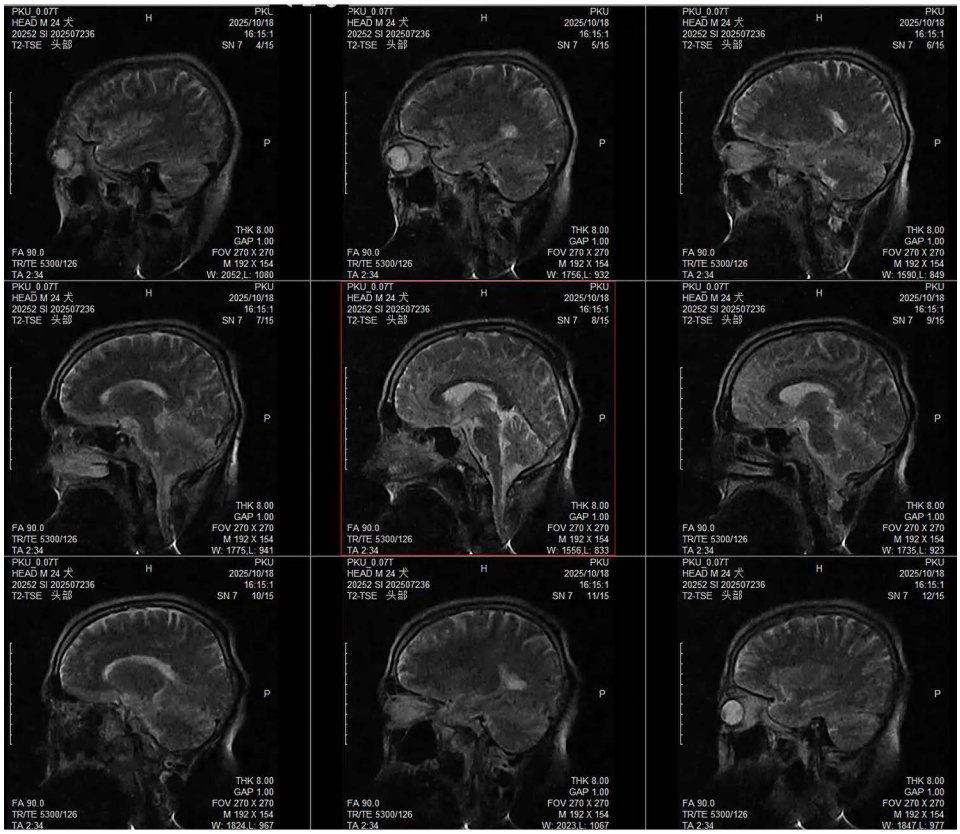


Fig. 6. Effect diagram of MRI solution imaging of MRI magnet system composed of hybrid magnetic circuit.

4. Conclusion

In conclusion, building upon theoretical simulations, we developed a rectangular-frame low-field MRI magnet system by hybridizing sintered Nd–Fe–B magnets with high remanence and sintered Sm–Co magnets with high remanence temperature coefficient. This system achieves both lightweight design and good temperature performance. The total weight of the magnet system is below 400 kg, while the magnetic field inhomogeneity at the boundary increases from 580 ppm to a maximum of only 1413 ppm, a rise of less than 833 ppm, over a temperature variation of ± 4 °C around the set point of 24 °C.

Acknowledgements

Project supported by the National Key Research and Development Program of China (Grant Nos. 2023YFB3507000 and 2021YFB3500300), the National Natural Science Foundation of China (Grant No. 52171167), partially supported by the Scientific Research Foundation of the Higher Education Institutions for Distinguished Young Scholars in Anhui Province, China (Grant No. 2022AH020012), the Innovation Project for Overseas Researcher in Anhui Province, China (Grant No. 2022LCX004), and the Facilities at Center of Free Electron Laser and High Magnetic Field (FEL & HMF) in Anhui University.

References

[1] Fuchs V R and Sox H C Jr 2001 *Health Aff.* **20** 30

[2] Edelman R R and Warach S 1993 *N. Engl. J. Med.* **328** 708

[3] Zhao Y J, Ding Y, Lau V, Man C, Su S, Xiao L F, Leong A T L and Wu E X 2024 *Science* **384** 636

[4] Liu Y L, Leong A T L, Zhao Y J, Xiao L F, Mak H K F, Tsang A C O, Lau G K K, Leung G K K and Wu E X 2021 *Nat. Commun.* **12** 7238

[5] Reilly T O, Teeuwisse W M, Gans D, Koolstra K and Webb A G 2021 *Magn. Reson. Med.* **85** 495

[6] Hennig J 2023 *Magn. Reason. Mater. Phys.* **36** 335

[7] Arnold T C, Freeman C W, Litt B and Stein J M 2023 *J. Magn. Reson. Imaging* **57** 25

[8] Sarracanie M, LaPierre C D, Salameh N, Waddington D E J, Witzel T and Rosen M S 2015 *Sci. Rep.* **5** 15177

[9] Kraus R, Espy M, Magnelind P and Volegov P 2014 *Ultra-low-field Nuclear Magnetic Resonance: A New MRI Regime* (Online: Oxford University Press)
[10] Campbell-Washburn A E, Ramasawmy R, Restivo M C, Bhattacharya I, Basar B, Herzka D A, Hansen M S, Rogers T, Bandettini W P, McGuirt D R, Mancini C, Grodzki D, Schneider R, Majeed W, Bhat H, Xue H, Moss J, Malayeri A A, Jones E C, Koretsky A P, Kellman P, Chen M Y, Lederman R J and Balaban R S 2019 *Radiology* **293** 384
[11] Zhang Y X, Kong X H, He W and Xu Z 2024 *IEEE Trans. Instrum. Meas.* **74** 4003909
[12] Liu Y, Xiao X, Kong X Z, Chen G Q, Zhou J N, Lu F Q, Zhao P F, Pang Y W and Wang Z C 2025 *Med. Phys.* **52** 2874
[13] Zhang T L, Zhang B, Wang H, He Y K, Xu C, Wang X Q, Zhang W, Zhang Z H and Jiang C B 2018 *J. Magn. Magn. Mater.* **466** 38
[14] Zhang X F, Liu L B, Li Y Q, Zhang D T, Liu W Q and Yue M 2024 *Chin. Phys. B* **33** 097503
[15] Shen P, Qian H D, Han J Z, Liu T, Yan Z, Ji M, Zhou L, Liu W Q, Liu S Q, Yang W Y, Li Y, Cao H H, Yue M, Yang J B and Yang Y C 2025 *Chin. Phys. B* **34** 087503
[16] Huang M, Ding Y, Zhao Z H, Wang C G, Zhou B, Liu L, Sun Y L and Yan A R 2024 *Chin. Phys. B* **33** 117503
[17] Bi Y F, Zheng M, Wang C, Wang L, Li Y C, Zhang B X, Fang Y K, Han W and Li W 2026 *J. Mater. Res. Technol.* **40** 2764
[18] Kimberly W T, Sorby-Adams A J, Webb A G, Wu E X, Beekman R, Bowry R, Schiff S J, de Havenon A, Shen F X, Sze G, Schaefer P, Iglesias J E, Rosen M S and Sheth K N 2023 *Nat. Rev. Bioeng.* **1** 617
[19] Mazurek M H, Cahn B A, Yuen M M, Prabhat A M, Chavva I R, Shah J T, Crawford A L, Welch E B, Rothberg J, Sacolick L, Poole M, Wira C, Matouk C C, Ward A, Timario N, Leasure A, Beekman R, Peng T J, Witsch J, Antonios J P, Falcone G J, Gobeske K T, Petersen N, Schindler J, Sansing L, Gilmore E J, Hwang D Y, Kim J A, Malhotra A, Sze G, Rosen M S, Kimberly W T and Sheth K N 2021 *Nat. Commun.* **12** 5119
[20] Lother S, Schiff S J, Neuberger T, Jakob P M and Fidler F 2016 *Magn. Reson. Mater. Phys.* **29** 691
[21] Cooley C Z, McDaniel P C, Stockmann J P, Srinivas S A, Cauley S F, Śliwiak M, Sappo C R, Vaughn C F, Guerin B, Rosen M S, Lev M H and Wald L L 2021 *Nat. Biomed. Eng.* **5** 229
[22] Philip K L, Qiu Y Q, Wang C Y and Zhang Z Y 2026 *Magn. Reson. Med.* **95** 188